LASER INTERFEROMETER GRAVITATIONAL WAVE OBSERVATORY
- LIGO -
CALIFORNIA INSTITUTE OF TECHNOLOGY
MASSACHUSETTS INSTITUTE OF TECHNOLOGY

Document Type **LIGO-T970072-01 - D** 4/2/97

Core Optics Support Conceptual Design

Michael Smith

Distribution of this draft:

This is an internal working note
of the LIGO Project.

California Institute of Technology
LIGO Project - MS 51-33
Pasadena CA 91125
Phone (818) 395-2129
Fax (818) 304-9834
E-mail: info@ligo.caltech.edu

Massachusetts Institute of Technology
LIGO Project - MS 20B-145
Cambridge, MA 01239
Phone (617) 253-4824
Fax (617) 253-7014
E-mail: info@ligo.mit.edu

WWW: http://www.ligo.caltech.edu/

1 PRODUCT PERSPECTIVE

A schematic layout of the detector assembly is shown in the figure 1, indicating the physical relationship of the COS subsystem components to the rest of the detector system.

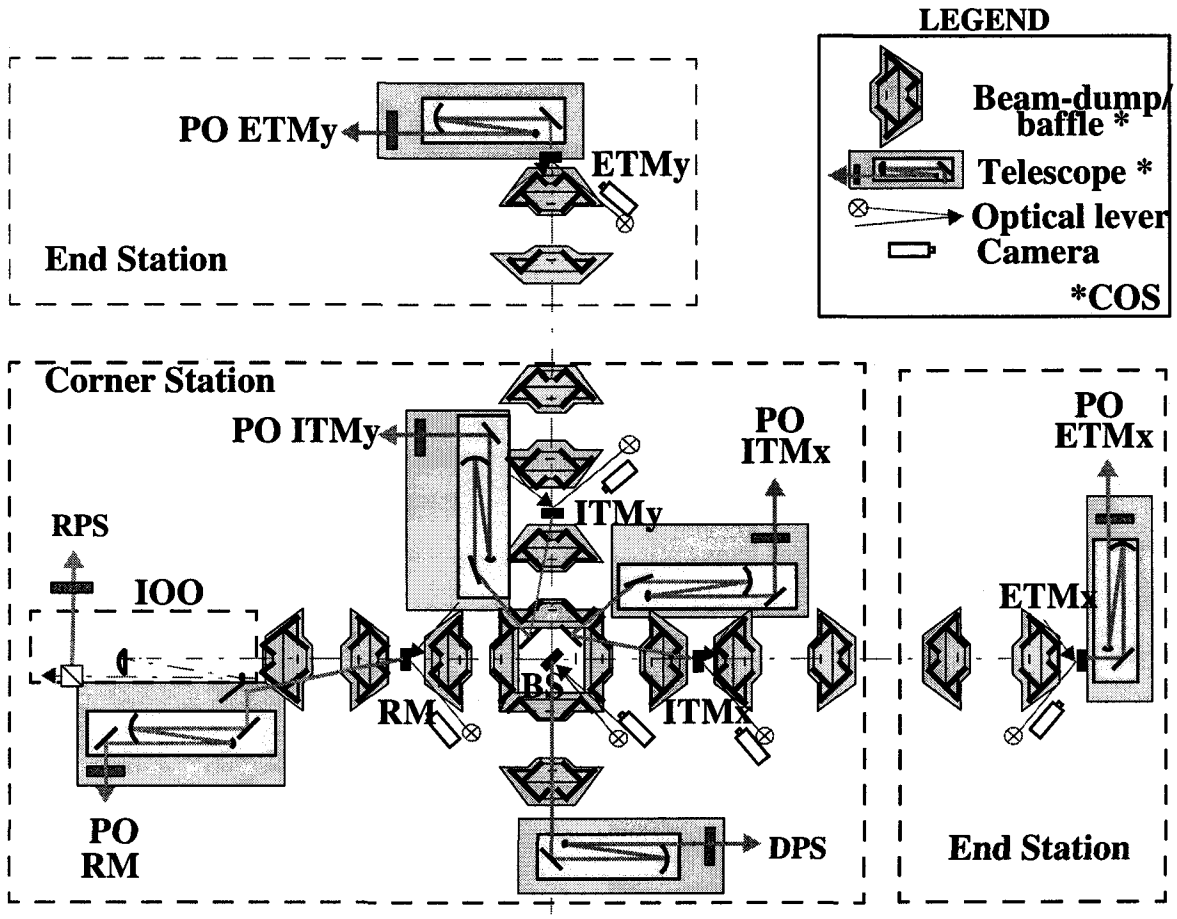

Figure 1: Core Optics Support Subsystem Elements- Schematic Layout

1.1. Ghost Beam Designation

The ghost beams created by the wedge surface of the COC are numbered according to the schematic shown following. The first surface reflection is designated 1 and is used as the pick-off beam. The main beam is designated 2. The ghost beams leaving the AR coated wedge surface are designated GB3, etc. The ghost beams leaving the mirror side of the COC are designated GB3b, etc.

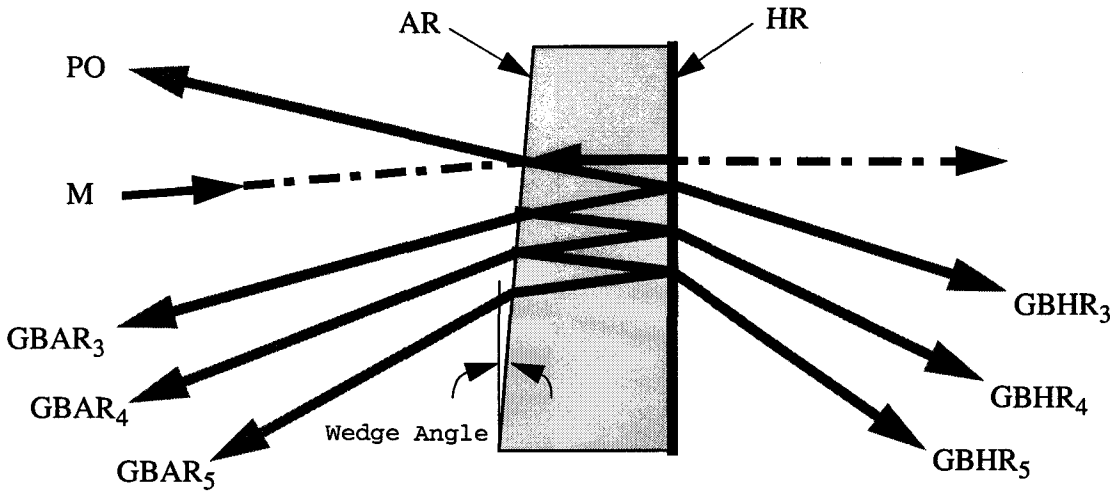

Figure 2: Ghost Beam Designation

2 BEAM-DUMPS AND BAFFLING OF COC

2.1. General

Specular ghost beams originate from internal reflections within the COCs due to the wedged substrate. Beam-dumps with low-scattering absorbing surfaces are used to attenuate the unwanted ghost beams. Each beam-dump consists of two pairs of surfaces, one pair on each side of the COC. One set of surfaces of the AR pair is located immediately adjacent to the AR side of the COC to attenuate $GBAR_5$ and higher angle beams; and the other set of the AR pair at the neighboring optics platform on the AR side of the COC to attenuate the $GBAR_3$, and $GBAR_4$. Likewise, there is a pair of beam-dump surfaces on the HR side of the COC. The set immediately adjacent to the HR side of the COC will attenuate the GBHR5 and higher beams, and the set located on the neighboring platform on the HR side of the COC will attenuate the $GBHR_3$, and $GBHR_4$ beams. The BS will have two pairs of beam-dumps for the x-beam and two paris of beam dumps for the y-beam.

A surrounding baffle is incorporated together with the beam-dump to attenuate the diffusely scattered light from the surfaces of the COC. The baffles function as a beam stop for all optical rays which lie outside the diameter of the COC.

2.2. RM Beam-dump/Baffle

2.2.1. RM Physical Configuration

The RM-baffle will consist of two beam-dump/baffle elements, as shown in figure 3, mounted on HAM3 optical table to control $GBAR_5$, $GBHR_5$ and higher order ghost beams; a beam-dump/baffle element mounted on HAM2 for $GBAR_3$, and $GBAR_4$; and a beam-dump/baffle element located on the neighboring platform BSC2 to catch $GBHR_3$ and $GBHR_4$. See "Recycling mirror beam-dump/baffle concept, showing pick-off beam telescope" on page 4.

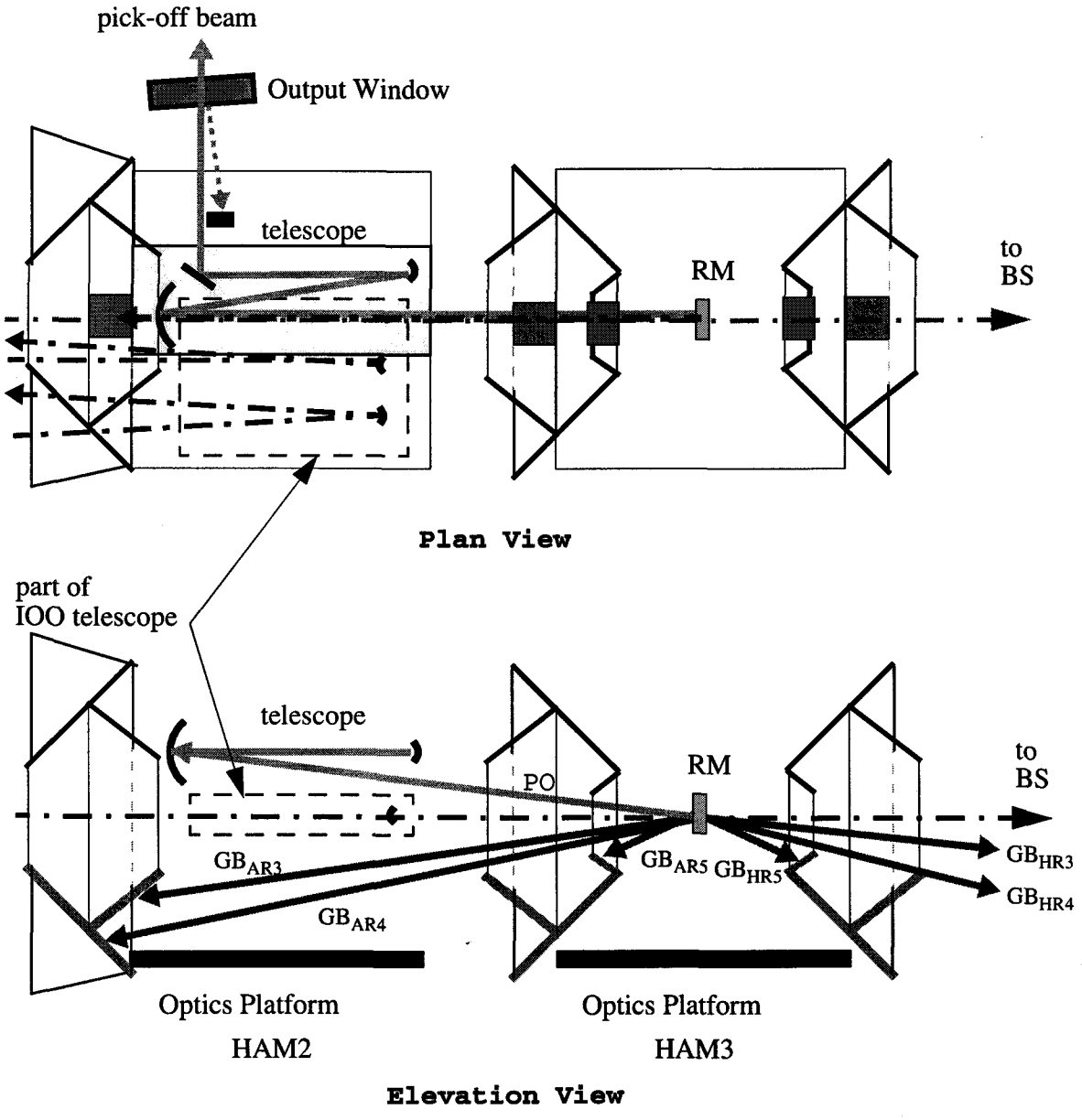

Figure 3: Recycling mirror beam-dump/baffle concept, showing pick-off beam telescope

2.3. BS Beam-dump/Baffle

2.3.1. BS Physical Configuration

The baffle BS consists of four beam-dump/baffle elements mounted on the BSC2 SEI optical platform, one surrounding each of the four beam paths through the beam splitter, to control $GBAR_5$, $GBHR_5$ and higher order ghost beams. The other elements of the beam-dump/baffle pairs are mounted on neighboring platforms HAM3 and BSC1 to catch $GBAR_3$, and $GBAR_4$ beams; and on neighboring platforms HAM4 and BSC3 to catch the GBHR3 and GBHR4 beams, as shown in figures 4, and 5.

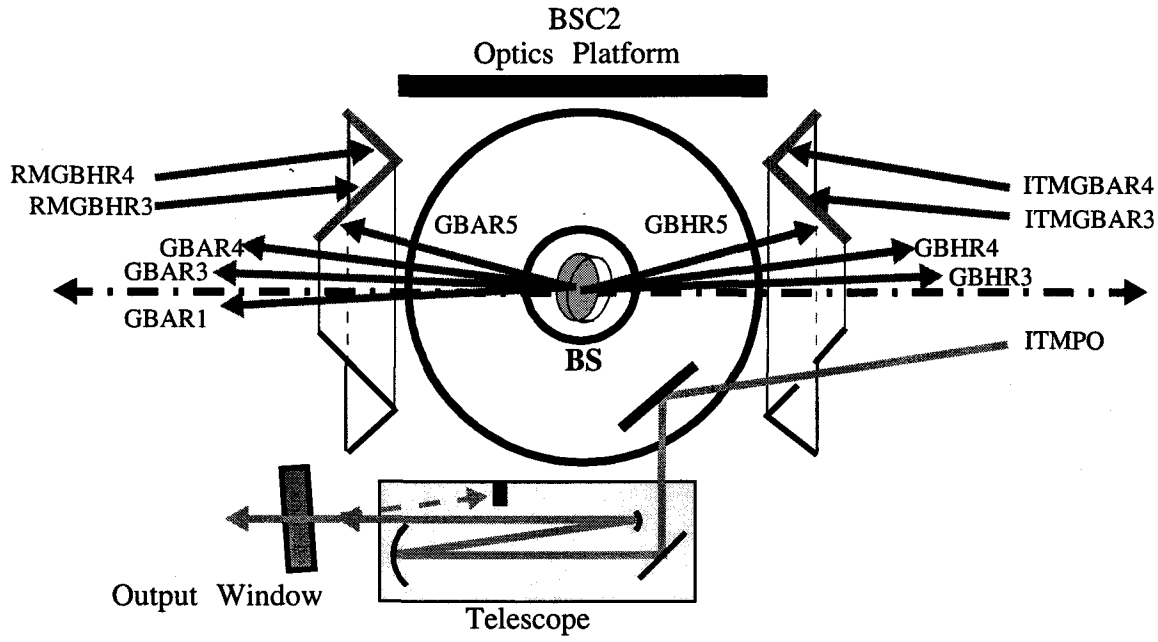

Figure 4: Elevation view of beam splitter beam-dump/baffle concept, with typical pick-off beam telescope and output vacuum window

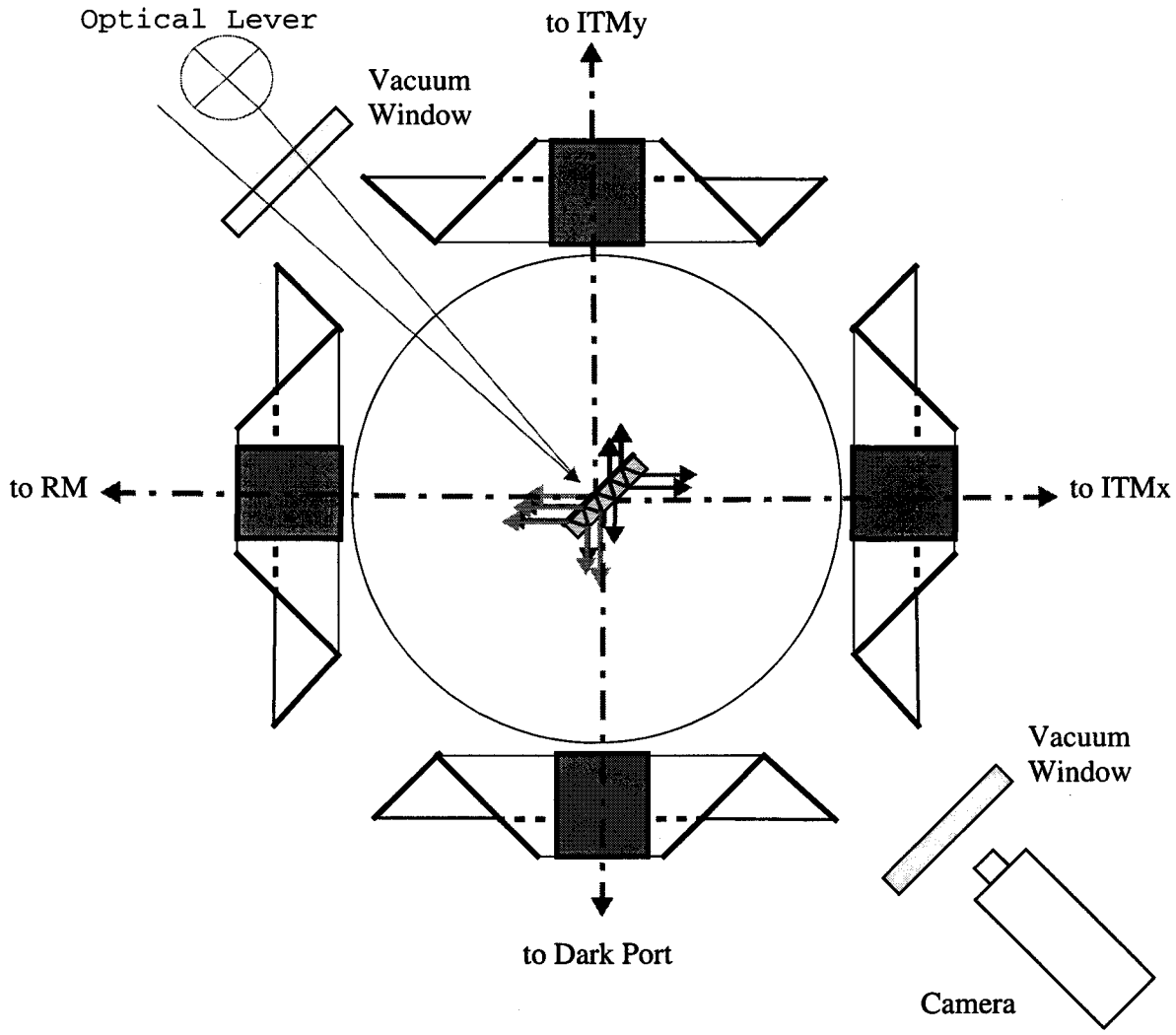

Figure 5: Plan view of beam splitter beam-dump/baffle concept, showing access for optical lever and TV camera viewing

2.3.1.1 2K BS $GBAR_3$ diffracted from the edge of the beam-dump mounted on the SEI platform into the recycling cavity

The 2K BS wedge angle is not large enough to cause the $GBAR_1$ and $GBAR_3$ beams from the BS to clear the RM. As shown typically in figure 6, part of $BSGBAR_3$ does not clear the RM mirror and is reflected back to the BS, with an additional reflection from BS to the neighboring beam-dump (not shown). A part of $GBAR_3$ will hit the edges of the BS and the BS beam-dump and will diffract into the solid angle of the IFO. The portion which diffracts from the BS edge causes negligible phase noise because the BS is suspended by the SUS pendulum. The portion which hits the edge of the BS beam-dump mounted on the SEI platform will diffract as a line source emitting a cylindrical wave. The diffracted light power can be estimated using Keller diffraction theory[1].

The geometry of the source will be approximated as an illuminated edge of length w, the gaussian beam parameter, and width of a few wavelengths, e.g. 3λ.

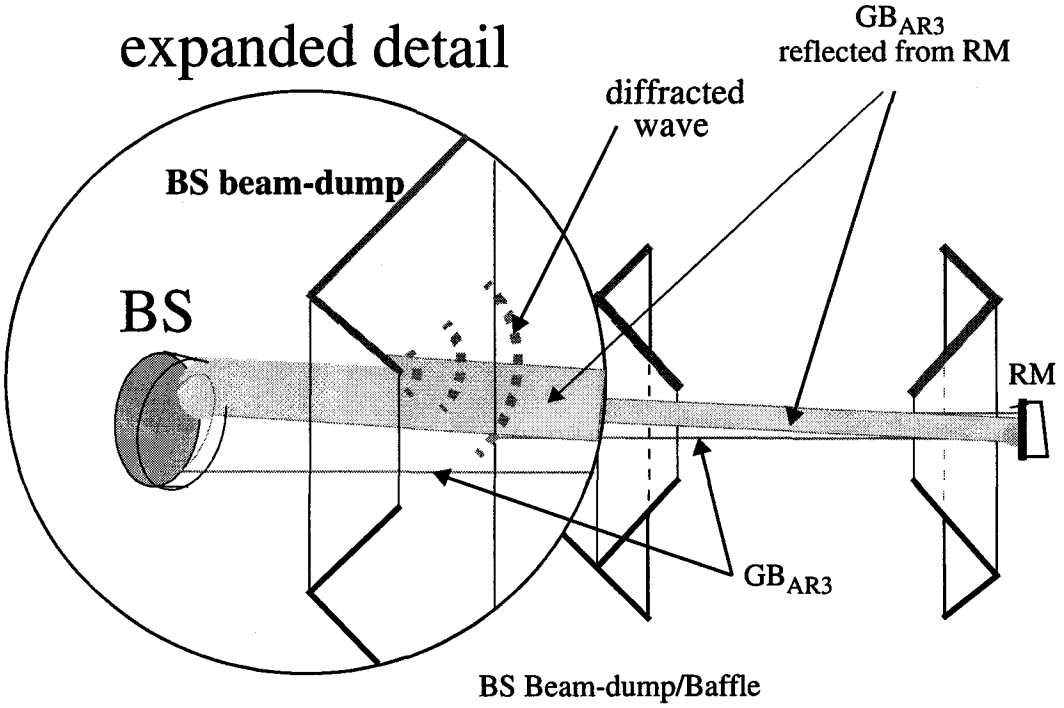

Figure 6: 2K BSGB Beam-dump Detail. Diffraction will occur at the edge of the BS and the BS beam-dump. See expanded detail.

This source will diffract predominately perpendicular to the illuminated edge and will generate a cylindrical wave covering approximately 3/4 of a cylinder into a solid angle measured at the distance L,

$$\Omega_d = \frac{3}{4} \cdot \frac{2\pi L w}{L^2} \text{ , sr}$$

The fractional power of the GB beam illuminating the edge is approximately

$$\frac{\Delta P}{P} = \frac{1}{w}\sqrt{\frac{2}{\pi}} \cdot 3\lambda \cdot \exp\left(-2 \cdot \frac{a^2}{w^2}\right) \text{ , and}$$

a is the Gaussian beam radius where the GB beam intercepts the edge.

The diffracted power into the IFO solid angle relative to the input laser beam is given by

1. private communication, Rai Weiss

$$\frac{P_{BSGBAR3dSEI}}{P_0} = R^2_{AR} \cdot \frac{G_{rc}}{2} \cdot \frac{1}{w}\sqrt{\frac{2}{\pi}} \cdot 3\lambda \cdot \exp\left(-2 \cdot \frac{a^2}{w^2}\right)\frac{2L}{3\pi w}\Delta\Omega = 3\times10^{-19}$$

2.4. ITM Beam-dump/Baffle

2.4.1. ITM Physical Configuration

The ITM 4K beam-dump/baffle will consist of two beam-dump/baffle elements mounted on BSC3/1 SEI optical table to control $GBAR_5$, $GBHR_5$ and higher order ghost beams; a beam-dump/baffle element mounted on the neighboring BSC2 SEI platform for $GBAR_3$, and $GBAR_4$; and a beam-dump/baffle element located on the neighboring platform BSC7/8 to catch $GBHR_3$ and $GBHR_4$, as shown in figure 7.

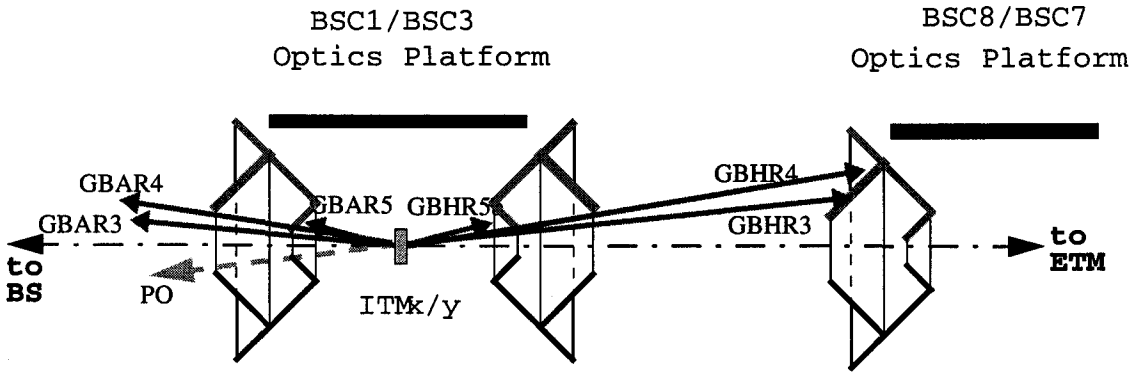

Figure 7: Elevation view of 4K ITM beam-dump/baffle concept

The ITM 2K beam-dump/baffle is identical to the ITM 4K except the baffle elements on the ETM side will be mounted to the vacuum housing inside the transition tubes WB-1B/WB-1A, as shown in figures 8 and 9.

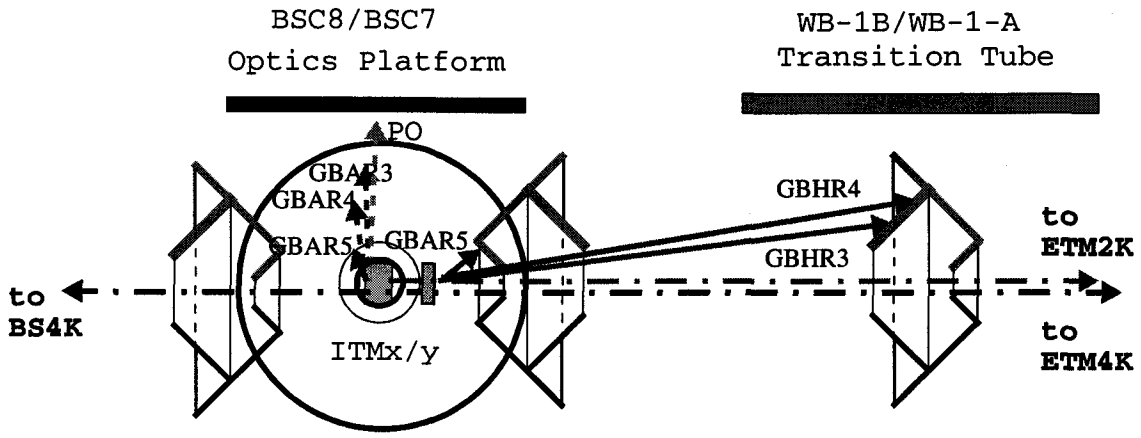

Figure 8: Elevation view of 2K ITM beam-dump/baffle concept

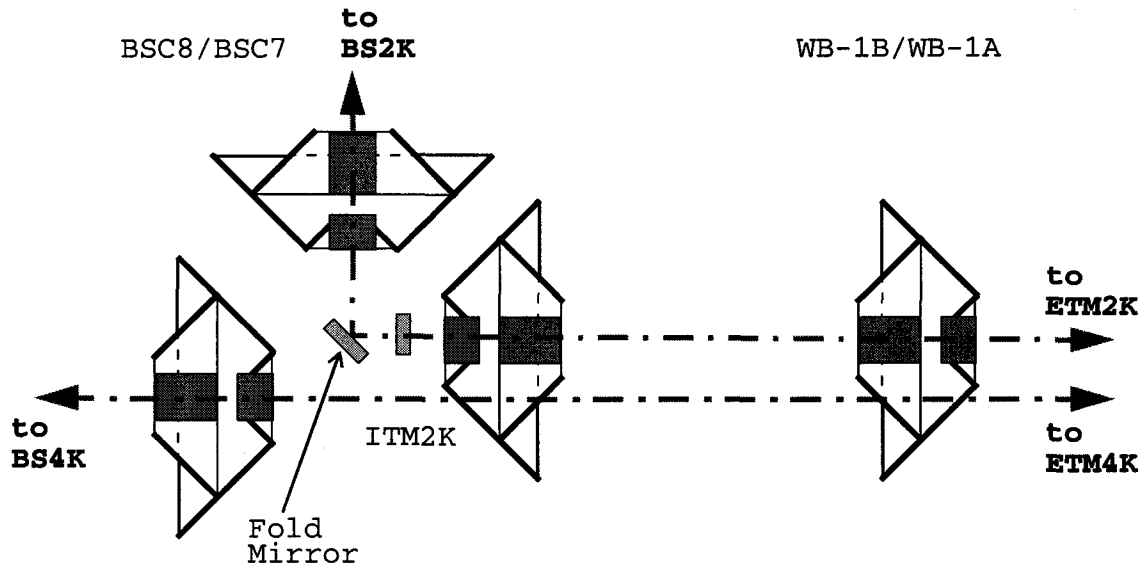

Figure 9: Plan view of 2K ITM beam-dump/baffle concept, showing passage of the 4K LIGO main beam

2.5. ETM Beam-dump/Baffle

2.5.1. ETM Physical Configuration

The ETM beam-dump/baffle will consist of two beam-dump/baffle elements mounted on the end chamber SEI optical table to control $GBAR_5$, $GBHR_5$ and higher order ghost beams; a beam-dump mounted on the output telescope assembly for $GBAR_3$, and $GBAR_4$; and a beam-dump/baffle element mounted to the inside of the beam tube transition section near the end chamber to catch $GBHR_3$ and $GBHR_4$, as shown in figure 10.

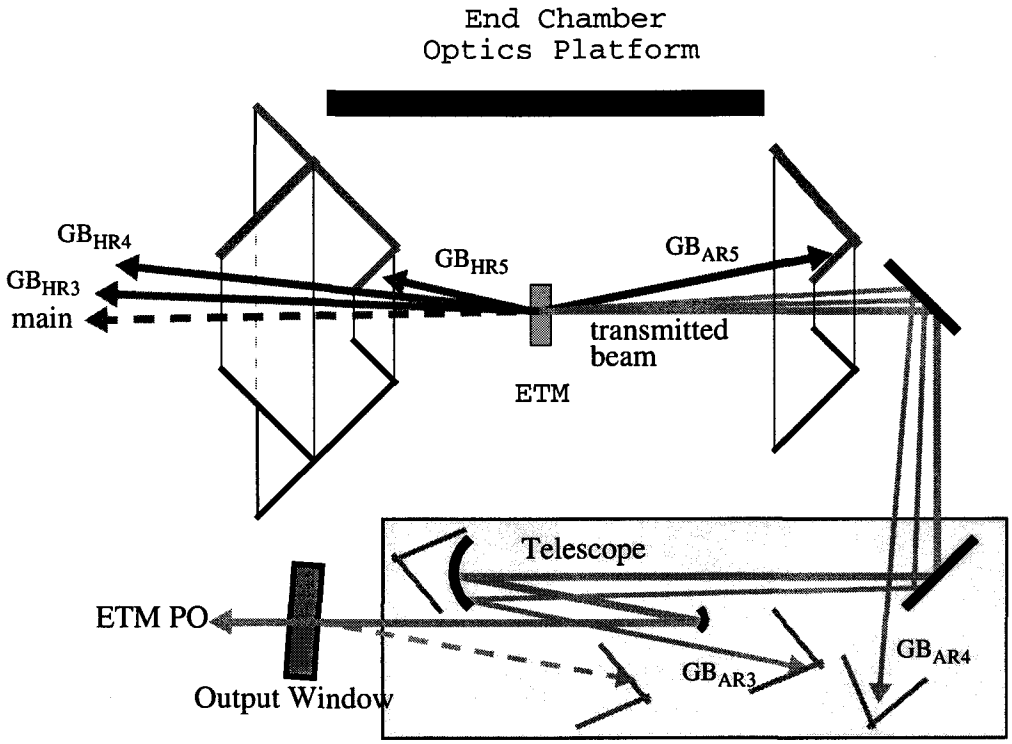

Figure 10: Elevation view of ETM beam-dump/baffle concept, with pick-off beam telescope and beam block to pass only the transmitted main beam

2.6. Summary of Scattered Light Intensities

The relative scattered light intensities were evaluated assuming the following parameters:

R_{RMAR} =.001
R_{RMHR} =.97
R_{BSAR} =.0001

R_{BSHR} =.50
R_{ITMAR} =.001
R_{ITMHR} =.97
R_{ETMAR} =.001
R_{ETMHR} =.999980
θ_{iwo} = 57 deg
θ_{ibd} = 57 deg
$BRDF_{wo} = 1x10^{-4}$ sr^{-1}
$BRDF_{bd} = 1x10^{-3}$ sr^{-1}
M_{ITMPO} = 0.1
M_{ETMPO} = 0.1
G_{rc} = 50
A_{Fi} =.001,
$T_{FP} = 2.6x10^{-3}$
w = 3.64 cm
a = 5.6 cm
L = 4.4 m
$\lambda = 1.06\times10^{-6}$m

$\Delta\Omega = 2.7\times10^{-10} sr$ is the solid angle of the IFO main beam which contains 86% of the Gaussian beam power, and

$\frac{P_{DPS}}{P_0} = 0.05$ is the ratio of DPS output power to the input laser power,

$\frac{P_{RPS}}{P_0} = 0.02$ is the ratio of RPS output power to the input laser power,

Table 1: Summary of 4K Scattered Light Calculations

source	*No. of beams*	*scattered power allocation factor*	*scattered power into IFO Ps, watts*	*Requirement per source Ps, watts*		
				30 Hz	*100 Hz*	*1000Hz*
ITMxPO-vh-rc	1	0.2685	1.8E-13	1.8E-13	1.8E-13	4.5E-08
ITMyPO-vh-rc	1	0.2685	1.8E-13	1.8E-13	1.8E-13	4.5E-08
BSDPS-vh-rc	1	0.2969	2.0E-13	2.0E-13	2.0E-13	4.9E-08
RPS-vh-rc	1	0.0002	1.0E-13	1.0E-13	1.0E-13	2.6E-08
ETMxPO-vh-acx			1.2E-11			

Table 1: Summary of 4K Scattered Light Calculations

ETMyPO-vh-acy			1.2E-11			
ETMxGBHR3-vh-acx			4.8E-34			
ETMyGBHR3-vh-acy			4.8E-34			
vh-ac subtotal	2	0.16588	2.5E-11	1.2E-11	1.2E-11	3.1E-06
BSGBAR3x-SEI-rc			2.2E-19			
BSGBAR1x'-SEI-rc			3.5E-20			
BSGBAR1x'-d-SEI-rc			9.9E-20			
BSGBAR3x'-SEI-rc			4.4E-21			
BSGBAR3y'-SEI-rc			4.4E-21			
ITMxGBAR3-SEI-rc			3.7E-17			
ITMyGBAR3-SEI-rc			3.7E-17			
BSGBHR3x-SEI-rc			2.2E-19			
BSGBHR3x'-SEI-rcs			2.2E-19			
BSGBHR3y'-SEI-rc			2.2E-19			
SEI-rc subtotal	2	0.000000	7.6E-17	6.3E-18	2.3E-16	2.3E-14
RMGBHR3-SEI-rcs	1	0.000000	2.6E-18	4.4E-19	1.6E-17	4.4E-15
RMPO-vh-lc	1		9.9E-17	1.00E-14	1.00E-14	1.00E-14

2.7. Beam-dump and Baffle Material

2.7.1. Beam-dump Surface Reflectivity

The surface of the beam dump will be composed of a slab of polished infra-red absorbing glass. The surface will be oriented at Brewster's angle with respect to the p-polarization of the specular ghost beam. The first reflectivity is expected to be < 0.001, and the ghost beam will undergo at least one more reflection with a reflectivity of <.04. Therefore, the net reflectivity of the ghost beam from the beam-dump apparatus is expected to be $< 4 \times 10^{-5}$. A schematic of the beam-dump concept is shown in figure 11.

2.7.2. Beam-dump Surface Scattering

The scattering requirements for the surface of the beam-dump were calculated in the COS DRD to be BRDF < 2π. However a considerable factor of safety will result if the surface has a BRDF < 0.001, which has been measured on a sample of commercial grade Schott IR absorbing glass.[1]

1. private communication Rai Weiss.

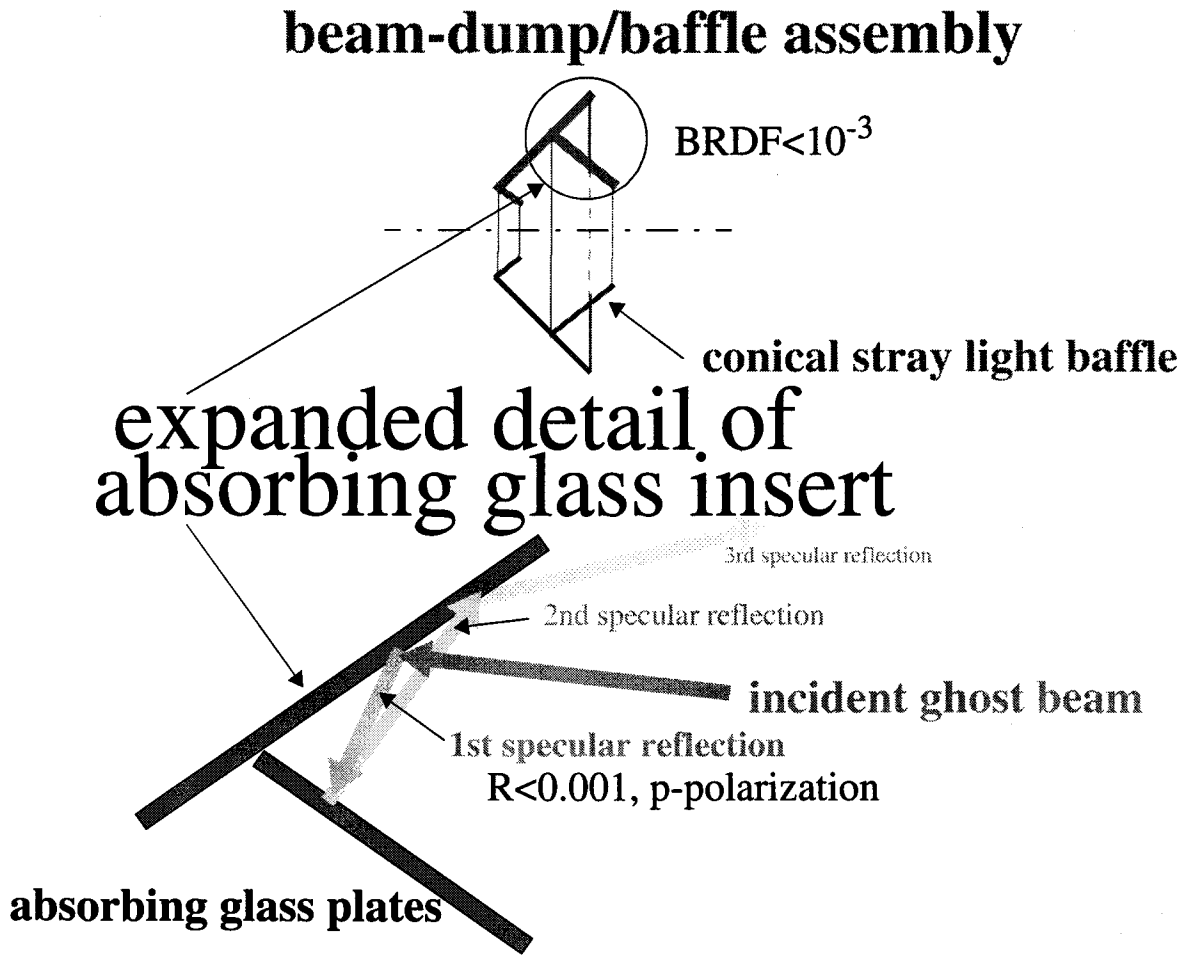

Figure 11: Beam-dump/baffle Concept

2.7.3. Beam Baffle Surface Scattering

The conical beam baffle surfaces will be fabricated from the oxidized stainless steel material which is being used for the beam-tube baffles. The surfaces will be tilted at approximately Brewster's angle to the stray light which has been scattered by the COC and by neighboring beam baffle surfaces. The tilt of the surfaces will avoid any parasitic cavity resonances between neighboring beam baffles.

2.8. Baffling of Support Optics

2.8.1. Baffle for Input Optics Telescope

A beam baffle will surround the output beam of the IOO telescope. This baffle will block any stray light generated on the IOO platforms which is headed toward the input port of the IFO.

3 SEPARATION OF GB AND PO BEAMS CAUSED BY WEDGED SURFACES OF CORE OPTICS

3.1. 4K IFO

The specified wedge angles of the 4K COC cause an adequate separation of the PO and GB beams from the main beam at the pick-off locations of > 7cm.

3.2. 2K IFO

The BS wedge is not large enough to cause a separation of the first order GB beams at the closest pick-off location which is at the RM. There is an over lap of 12.8 cm, which means that the GB has completely fallen back on the diameter of the RM. All of GBAR3 will hit the surface of the RM and will reflect back toward the BS. When the reflected GBAR3 reaches the BS location part of it will be caught by the BS beam-dump, and part will be reflected toward the ITM beam-dump, where it will be separated enough from the main beam and will be caught by the beam-dump. This is shown schematically in figure 6.

4 PO BEAM-REDUCING TELESCOPE DESIGN PARAMETERS

The PO beam diameter will be reduced by means of a telescope mounted on the appropriate optics platform within the vacuum enclosure, as shown in figure 12. The fold mirror shortens the overall length of the telescope to approximately 0.5 m. The specifications for the PO beam reducing telescopes are shown in Table 2 on page 15.

The aberrations caused by each off-axis mirror were described in terms of Zernike polynomials (See "APPENDIX: Zernike Polynomial Description of Mirror Distortion" on page 21.), and the aberrated wavefront was analyzed by WFS using modal analysis. A preliminary analysis by WFS indicated that total astigmatic and curvature aberrations $<\lambda/8$ peak-valley @ l=1.06 micron on each mirror would be acceptable. Higher order aberrations must be $< \lambda/40$. An analysis using Code V optical design software indicated that this would result in a total aberration of $<\lambda/4$ for the combined off-axis parabolic telescope.

The ETM PO beam is not used for wavefront sensing, so the aberrations are relatively unimportant. A much cheaper off-axis spherical telescope is proposed for the ETM PO beam, with a total p-v aberration of 5 lambda.

Table 2: Specifications for PO Beam Reducing Telescopes

Property	*Value*	
	RM, ITM, DPS	*ETM*
configuration	off-axis parabolic	off-axis spherical
primary radius, mm	1800	1800
secondary radius, mm	180	180
total curvature and astigmatism aberration	$<\lambda/4$ peak-valley @ λ=1.06 micron	$<5\lambda$ peak-valley @ λ=1.06 micron
total higher order aberrations	$<\lambda/20$ peak-valley @ λ=1.06 micron	$<1\lambda$ peak-valley @ λ=1.06 micron
input clear aperture diameter	156 mm	156 mm
output clear aperture diameter	15.6 mm	15.6 mm
Internal resonance and Q	TBD	TBD
output beam parameter	3.64 mm	3.64 mm
output beam waist location	TBD	TBD
magnification	0.1X	0.1X

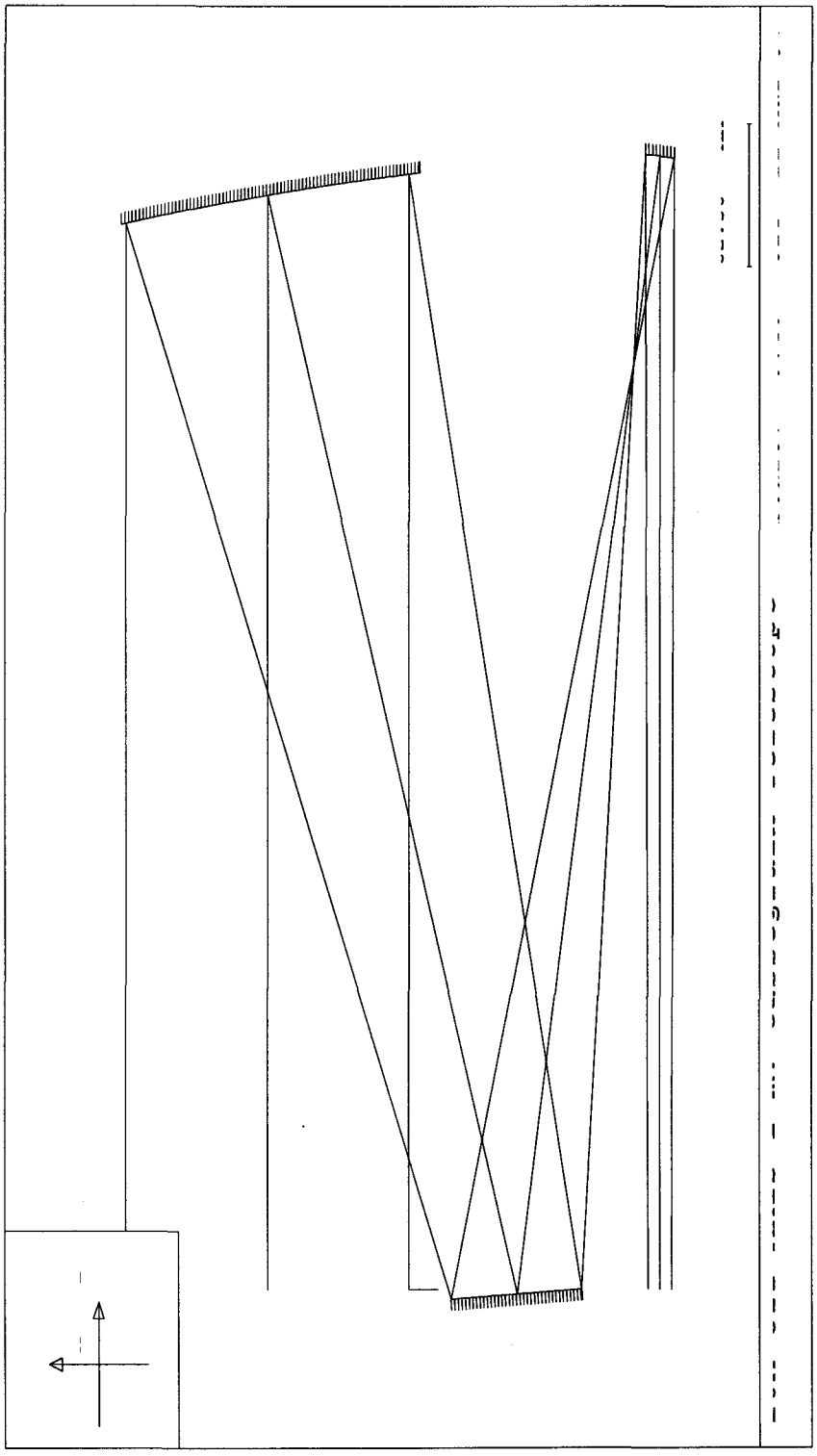

Figure 12: PO Beam Reducing Telescope

5 OUTPUT VACUUM WINDOW

Output vacuum windows will provide optical paths for PO beams out of the vacuum enclosure to interface with the ASC/LSC subsystems.

The surface figure of the window will cause an optical path difference (OPD) aberration of the beam wavefront. The total OPD for both surfaces is $OPD = 2 \cdot (1 - n) \cdot \Delta t$, where n is the index of refraction and Δt is the deviation from flatness of the surface. For a p-v surface deformation of $\Delta t = \lambda/20$ 'the window will add an aberration of$OPD = 0.045\lambda$, which will increase the wavefront aberration from 0.25λ to 0.30λ. This may be acceptable to WFS.

The specifications for the PO windows are summarized below.

Table 3: Requirements for PO Beam Vacuum Window

Property	*Value*
material	fused silica
thickness	TBD
substrate diameter	TBD
wedge	34° ± 5′
clear aperture	>20 mm
surface figure	λ/20 TBD per surface over clear aperture
AR coating, both surfaces	<.001 @1064 nm, @ 55.4° incidence angle, p polarization
$BRDF_{wo}$	$< 5x\ 10^{-2}\ sr^{-1}$
Vacuum properties	Vacuum Equipment Specification, LIGO-E940002-02-V

6 INITIAL OPTICAL ALIGNMENT OF IFO

The COS optical beam-dump/baffles will be removable in order to facilitate the initial alignment of the IFO. The baffles will be mounted to a reference bracket so they may be removed and subsequently replaced in the same position without requiring realignment.

7 RESONANT FREQUENCY OF COS ELEMENTS MOUNTED ON THE OPTICS PLATFORM

The beam-dump/baffle assembly will have stiffening ribs with sufficiently high moment of inertia so that the TBD resonant frequency of the beam-dump/baffle together with the Q of the structure will not add excessive thermal-noise to the SEI optical platform. See the design approaches for reducing thermal noise in the Seismic Isolation DRD, LIGO-T960065-02-D.

Likewise, the mounting structure for the telescope mirrors and steering mirrors will be sufficiently rigid, with damping, so as not to add excessive thermal-noise to the SEI optical platform.

8 ENGINEERING MOCK-UP

A mock-up of the BSC2 chamber will be constructed to facilitate the final design of the COS. The actual configuration and placement of COS elements is intimately dependent upon the location of COC suspension housings, and the actual paths of optical beams within the chamber. A full size mock-up will provide a sanity check on possible interference of the beam-dump baffles, and other bulky COS elements with other IFO elements. The mock-up will also provide valuable information necessary for the implementation of workable IFO initial alignment procedures.

9 ENGINEERING TEST PLANS

9.1. Receiving Inspection

All received optical parts; which will include telescope mirrors, folding mirrors, output windows, black glass beam-dump material, and dark-oxidized baffles will undergo a visual receiving inspection.

The receiving inspection will verify that the optical elements meet the appropriate scratch and dig, and other surface qualify specifications.

9.2. Engineering Tests

9.2.1. Alignment of PO Telescopes

A test apparatus will be used to pre-align the telescope mirrors onto the sub-mounting assembly to which they will be mounted.

9.2.2. BRDF measurement of beam-dump surfaces.

A BRDF apparatus will be used to verify that the surfaces of the telescope mirrors, the output window, and the beam-dump black glass material meet the BRDF specifications.

APPENDIX 1 APPENDIX: SCATTERING FROM FRACTAL SURFACES

10

10.1. Fractal Model of Surface Scattering BRDF

The angular dependence of scattering from polished optical surfaces can be modeled reasonably well with the fractal expression below.

$$BRDF(\ ) = \frac{a}{(\quad)^c}$$

LIGO superpolished COC surfaces have measured values of the constants (verbal communication Albert L.) $a = 2.5\times10^5$, $b = 2\times10^{10}$, $c = 1.5$. For most surfaces, the constant c is of order unity.

10.2. Scattered Light Fraction

The scattered light fraction is determined by integrating the BRDF over the appropriate scattering solid angle. The surface may be tilted at an angle θ_t.

$$\frac{P_s}{P_i} = \cos\theta_i \cdot \int_{\phi_1\theta_1}^{\phi_2\theta_2}\int \frac{a}{(\quad)^c}\cdot d\theta d\phi$$

The appropriate solid angle for backscattering into the IFO is the coherence cone of the IFO,

$$\Delta\Omega = \pi\cdot\left(\quad\right)^2 = \frac{\lambda^2}{\pi w_0^2}$$

In order to simplify the math, we will assume that the angles are small, and that c=1. A small angle approximation is valid for tilt angles up to approximately 10 degrees.

Then, the integral can be performed exactly

$\frac{P_s}{P_i} = \Delta\phi\cdot\frac{a}{2b}\log\left(\quad\right)$, where log will be used as the symbol for ln.

The results for two different cases are presented below: 1) backscattering in the specular direction from a surface at normal incidence, and 2) backscattering at large angles to the specular direction.

Large angle scattering occurs whenever the surface is tilted by an angle that is much larger than the backscattering acceptance angle, which is simply the divergence half-angle of the IFO beam and is approximately $\Delta\theta = 1\times10^{-5}$ rad.

$\theta_t \gg \Delta\theta$, and $b\theta^2 \gg 1$.

10.2.1. Numerical Results

Numerical results for the scattered light fraction are presented below, for the two cases.The calculations assumed the following surface parameters, which are characteristic of COC superpolished optics, and are not necessarily representative of "good" commercial surfaces.

$a = 2.5\times10^{5}$

$b = 2\times10^{10}$, and

$\Delta\Omega = 6.7\times10^{-10} sr$

wavelength=1.06E-06, m

gaussian spot size=0.0364, m
maximum scattering angle=1.854E-05

Table 4: Scattering from Fractal Surfaces

	NORMAL INCIDENCE	*TILTED SURFACE*			
	scattered light fraction				
tilt angle, deg	0	1	2	5	10
tilt angle, rad	0	0.0175	0.0349	0.0873	0.1745
magnification					
1.000	6.48E-05	2.19E-11	5.47E-12	8.75E-13	2.19E-13
0.707	8.45E-05	4.37E-11	1.09E-11	1.75E-12	4.37E-13
0.500	1.05E-04	8.75E-11	2.19E-11	3.50E-12	8.75E-13
0.354	1.26E-04	1.75E-10	4.37E-11	7.00E-12	1.75E-12
0.250	1.48E-04	3.50E-10	8.75E-11	1.40E-11	3.50E-12
0.177	1.70E-04	7.00E-10	1.75E-10	2.80E-11	7.00E-12
0.125	1.91E-04	1.40E-09	3.50E-10	5.60E-11	1.40E-11
0.088	2.13E-04	2.80E-09	7.00E-10	1.12E-10	2.80E-11

Table 4: Scattering from Fractal Surfaces

0.063	2.35E-04	5.60E-09	1.40E-09	2.24E-10	5.60E-11
0.044	2.57E-04	1.12E-08	2.80E-09	4.48E-10	1.12E-10
0.031	2.78E-04	2.24E-08	5.60E-09	8.96E-10	2.24E-10
0.022	3.00E-04	4.48E-08	1.12E-08	1.79E-09	4.48E-10
0.014	**3.29E-04**	**1.13E-07**	**2.83E-08**	**4.53E-09**	**1.13E-09**
0.010	3.51E-04	2.27E-07	5.67E-08	9.07E-09	2.27E-09
0.007	3.73E-04	4.53E-07	1.13E-07	1.81E-08	4.53E-09

As the table shows, a significant reduction of backscattered light is achieved by tilting the surface a small amount. The m=0.014 data corresponds to the COS BRDF calculations for the demagnified PO beam scattering.

APPENDIX 2 APPENDIX: ZERNIKE POLYNOMIAL DESCRIPTION OF MIRROR DISTORTION

11

11.1. Introduction

The primary aberrations on the surface of a tilted telescope mirror are described in terms of the Zernike polynomial coefficients. The deviation of the reflected beam wavefront from the shape of a reference sphere is described as a function of the Zernike coefficients and the cartesian coordinates x, and y measured from the center of the mirror. w is the Gaussian beam spot radius. VZ_i are the Code V numbering of the Zernike coefficients. The Code V coefficients correspond to the Zernike designations, as shown in Table 5, "Code V and Zernike Coefficients," on page 23.

The Zernike coefficients for the primary and secondary mirrors of an off-axis spherical telescope, and an off-axis parabolic telescope are listed in Table 6, "Fringe Zernike Polynomial Coefficients:10X Off-axis Spherical Mirror Cassegrain Telescope, 125mm beam displacement, R1=3600mm R2=360mm, w1=36.4mm, w2=3.64mm, surface figure 1/4l astigmatism per surface," on page 24; and in Table 7, "Fringe Zernike Polynomial Coefficients:10X Off-axis Parabolic Mirror Cassegrain Telescope, 125mm beam displacement, R1=1800mm R2=180mm, w1=36.4mm, w2=3.64mm, surface figure 1/4l astigmatism per surface," on page 25.

The Guoy phase shifts between the TEM_{00} and the TEM_{01} beams traversing from the IFO beam waist, through the telescope, to the input to the WFS are listed in Table 8, "Guoy Phase Shift of TEM00 relative to TEM01, from IFO to WFS," on page 26

The x, y coordinates are the normalized coordinates of a unit circle which covers the aperture of the mirror. For the present telescope, the semi-diameter of the mirror is 2.15w, where w is the gaussian beam spot. Then

$x = \frac{X}{2.15w}$, and

$y = \frac{Y}{2.15w}$.

The telescope mirror parameters are:

$D_1 = 156mm$

$D_2 = 15.6mm$

$w_1 = 36.4mm$

$w_2 = 3.64mm$

The radii of curvature of the mirrors, R_1 and R_1 are given in the Table titles.

11.2. Description of Zernike Displacements

Piston

$\Delta z_1 = VZ_1$

Distortion (tilt)

x-distortion

$\Delta z_2 = VZ_2 \cdot x$

y-distortion

$\Delta z_3 = VZ_3 \cdot y$

Curvature

$\Delta z_4 = \frac{1}{\sqrt{2}} \cdot VZ_4 \cdot (2 \cdot (x^2 + y^2) - 1)$

$r^2 = x^2 + y^2$

Astigmatism

x-astigmatism

$\Delta z_5 = VZ_5 \cdot x^2$

y-astigmatism

$$\Delta z_6 = (-1) \cdot VZ_6 \cdot y^2$$

Coma

x-coma

$$\Delta z_7 = VZ_7 \cdot (3 \cdot x^3 - 2x)$$

y-coma

$$\Delta z_8 = VZ_8 \cdot (3 \cdot y^3 - 2y)$$

Spherical

$$\Delta z_9 = \frac{1}{\sqrt{2}} \cdot VZ_9 \cdot (6 \cdot (x^2 + y^2)^2 - 6 \cdot (x^2 + y^2) + 1)$$

11.3. Correspondence Between Code V Coefficients and Zernike Coefficients

Table 5: Code V and Zernike Coefficients

Description	*Code V Coefficient*	*Zernike Coefficient*
Piston	VZ_1	A_{000}
x-distortion (tilt)	VZ_2	A_{111} (r)
y-distortion (tilt)	VZ_3	A_{111} (r)
field curvature	VZ_4	A_{120} (r)
x-astigmatism	VZ_5	A_{022} (r)
y-astigmatism	VZ_6	A_{000} (r)
x-coma	VZ_7	A_{031} (r)
y-coma	VZ_8	A_{031} (r)
spherical aberration	VZ_9	A_{040} (r)

11.4. Sample Mirror Wavefront Aberration Data

The wavefront aberration was calculated using Code V optical design program, for two cases: 1) see Table 6, "Fringe Zernike Polynomial Coefficients:10X Off-axis Spherical Mirror Cassegrain Telescope, 125mm beam displacement, R1=3600mm R2=360mm, w1=36.4mm, w2=3.64mm, surface figure 1/4l astigmatism per surface," on page 24, and 2) seeTable 7, "Fringe Zernike Polynomial Coefficients:10X Off-axis Parabolic Mirror Cassegrain Telescope, 125mm beam displacement, R1=1800mm R2=180mm, w1=36.4mm, w2=3.64mm, surface figure 1/4l astigmatism per surface," on page 25

Table 6: Fringe Zernike Polynomial Coefficients:10X Off-axis Spherical Mirror Cassegrain Telescope, 125mm beam displacement, R_1=3600mm R_2=360mm, w_1=36.4mm, w_2=3.64mm, surface figure 1/4λ astigmatism per surface

Code V Coefficient	*Value*	
	R1=3600mm	*R2=360mm*
VZ_1	1.1600	0.2304
VZ_2	0.0001	0.0001
VZ_3	0.8096	0.0797
VZ_4	1.1914	0.2335
VZ_5	-0.9704	-0.0976
VZ_6	0.1267	0.1267

Table 6: Fringe Zernike Polynomial Coefficients:10X Off-axis Spherical Mirror Cassegrain Telescope, 125mm beam displacement, R_1=3600mm R_2=360mm, w_1=36.4mm, w_2=3.64mm, surface figure 1/4λ astigmatism per surface

Code V Coefficient	*Value*	
	R1=3600mm	*R2=360mm*
VZ_7	0.0001	0.0001
VZ_8	0.4055	0.0408
VZ_9	0.0314	0.0031

Table 7: Fringe Zernike Polynomial Coefficients:10X Off-axis Parabolic Mirror Cassegrain Telescope, 125mm beam displacement, R_1=1800mm R_2=180mm, w_1=36.4mm, w_2=3.64mm, surface figure 1/4λ astigmatism per surface

Code V Coefficient	*Value*	
	R1=1800mm	*R2=180mm*
VZ_1	0.1334	0.1334
VZ_2	0.0006	0.0006
VZ_3	-0.0058	-0.0058
VZ_4	0.1332	0.1332
VZ_5	-0.0025	-0.0025
VZ_6	0.1321	0.1321
VZ_7	0.0003	0.0003
VZ_8	0.0011	0.0011
VZ_9	-0.0002	-0.0002

The aberrations from the off-axis spherical mirror telescope appear to be excessive, simply due to the off-axis spherical surfaces

The off-axis parabolic telescope creates aberrations only due to the actual surface figure of the mirrors, so the total aberration is considerably smaller than the spherical telescope.

11.5. Guoy Phase Shifts

IFO to Telescope Input Aperture

$$\Delta\phi_{IFO} = \text{atan}\frac{z_{IFO}}{z_{IFOR}}$$

$$z_R = \frac{\pi w_0^{\,2}}{\lambda}$$

Telescope Input Aperture to Output Aperture

$$\Delta\phi_{tel} = \pi$$

Telescope Output Aperture to WFS

$$\Delta\phi_{WFS} = \text{atan}\frac{z_{WFS}}{z_{telR}}$$

Table 8: Guoy Phase Shift of TEM_{00} relative to TEM_{01}, from IFO to WFS

Path	$\Delta\phi$	w_0	z_R	z
IFO to input aperture	0.244	0.0351	$3.7\text{x}10^{3}$	970
input aperture to output aperture	3.142	$9.3\text{x}10^{-6}$	$2.55\text{x}10^{-4}$	1
output aperture to WFS	0.051	0.00364	39	2
Total phase shift	3.437			